Research Article Vol. 58, No. 13 / 1 May 2019 / Applied Optics 3359

applied optics

Progressive scheme for blending empirical ocean color retrievals of absorption coefficient and chlorophyll concentration from open oceans to highly turbid waters

SHAOLING SHANG,[1,2,4] ZHONGPING LEE,[3,5] GONG LIN,[1] YONGHONG LI,[1,2] AND XUE LI[1]

[1]State Key Laboratory of Marine Environmental Science, College of Ocean and Earth Sciences, Xiamen University, Xiamen 361102, China
[2]Key Laboratory of Underwater Acoustic Communication and Marine Information Technology (Xiamen University), Ministry of Education of China, Xiamen 361102, China
[3]School for the Environment, University of Massachusetts Boston, Boston, Massachusetts 02125, USA
[4]e-mail: slshang@xmu.edu.cn
[5]e-mail: zhongping.lee@umb.edu

Received 14 November 2018; revised 25 March 2019; accepted 25 March 2019; posted 26 March 2019 (Doc. ID 351652); published 25 April 2019

To achieve a smooth transition between algorithms for "clear" water and "turbid" water, we propose a single formula to calculate the input parameter (ip) used for empirical retrieval of absorption coefficients (a) or chlorophyll concentration ([Chl]) from remote-sensing reflectance (R_{rs}). This formula for ip takes the ratio of the maximum R_{rs} in the blue-green bands to the sum of R_{rs}(green) and the scaled R_{rs} in the red and infrared bands (termed as $ip_{\text{Max-Sum}}$). We found that, compared to the widely used OC4-type formula for ip, $ip_{\text{Max-Sum}}$ can improve the coefficient of determination from ∼0.88 to 0.99 for absorption coefficient at 440 nm [$a(440)$] in ∼0.01–20.0 m^{-1} ([Chl] ∼0.01–500 mg m^{-3}). Especially, the sensitivity of $ip_{\text{Max-Sum}}$ to the change in $a(440)$ is about five times greater than that of OC4-type for $a(440) > \sim 1.0\ \text{m}^{-1}$ ([Chl] $> \sim 10\ \text{mg m}^{-3}$). These results indicate an advantage of $ip_{\text{Max-Sum}}$ for generating robust and seamless $a(440)$ or [Chl] from clear to highly turbid waters. The inclusion of such a scheme in a quasi-analytical algorithm is also presented.

https://doi.org/10.1364/AO.58.003359

1. INTRODUCTION

Optical properties and phytoplankton concentration are not only indices of the status of oceanic waters [1,2], but also play important roles in the physical and biological processes that modulate the ocean–atmosphere system [3,4]. Due to the enormous area of the world oceans, remote sensing via satellites is the means to obtain repeated synoptic observations of ocean properties. For this goal, in addition to sensor calibration and atmospheric corrections, one important aspect is to have robust algorithms to obtain water properties from satellite-derived ocean color. In the past decades, various empirical and semi-analytical algorithms have been developed to retrieve chlorophyll concentration ([Chl], mg m^{-3}) and the absorption coefficient (a, m^{-1}) [5–7]. Due to their simplicity and long heritage in processing satellite ocean color data, empirical algorithms are still the dominant scheme for obtaining [Chl] of the global oceans. This is because, starting about four decades ago [8], the spectral ratio of water color, represented by either water-leaving radiance or remote-sensing reflectance (R_{rs}, sr^{-1}), between the blue (∼440 nm) and green (∼550 nm) bands is a good indication of [Chl] in oceanic waters. We may term this ratio as a blue-green input parameter ($ip_{\text{blue-green}}$) for an empirical algorithm. This strategy became the heritage blue-green ratio algorithm (BGRA) for [Chl] [9,10] and the diffuse attenuation coefficient of downwelling irradiance (K_d, in m^{-1}) [11], with the current version (OC4) taking a form using the maximum among $R_{rs}(443), R_{rs}(490)$, and $R_{rs}(510)$ to ratio $R_{rs}(555)$ as the input parameter, or ip (for SeaWiFS, as an example), as shown below:

$$\log([\text{Chl}]) = \beta_0 + \beta_1 \times RR + \beta_2 \times RR^2 + \beta_3 \times RR^3 + \beta_4 \times RR^4, \quad \textbf{(1a)}$$

$$RR = \log\left(\frac{\text{Max}(R_{rs}(443, 490, 510))}{R_{rs}(555)}\right). \quad \textbf{(1b)}$$

Here, β_{0-4} are algorithm coefficients tuned based on data collected from field measurements [5], and there are slight variations in values (https://earthdata.nasa.gov/) for different ocean color satellites (e.g., MODIS and MERIS) in order to take into account the variation in central wavelengths of sensors (e.g., 555 nm for SeaWiFS versus 560 nm for MERIS) and bandwidths. The resulted [Chl] values of global oceans, in general, are consistent among these satellite ocean color measurements. We may term the R_{rs} ratio in Eq. (1b) as $ip_{\text{Max-green}}$.

However, it has been found that such a ratio plateaus with the increase in constituents in water [12,13]. Figure 1 shows the total absorption coefficient at 440 nm $[a(440)]$ and [Chl] compared with $\text{Max}[(R_{rs}(\lambda))/R_{rs}(560)$, with $\text{Max}((R_{rs}(\lambda)]$ collectively representing the maximum among $R_{rs}(440)$, $R_{rs}(490)$, and $R_{rs}(510)$. When $a(440)$ becomes greater than $\sim 0.3\ \text{m}^{-1}$, ([Chl] is greater than $\sim 3\ \text{mg}\,\text{m}^{-3}$), the slope between $\log[\text{Max}(R_{rs}(\lambda))/R_{rs}(560)]$ and $\log[a(440)]$ becomes smaller and approaches 0 for $a(440)$ around $3.0\ \text{m}^{-1}$. This indicates that for water with a high absorption coefficient or high [Chl], $\text{Max}(R_{rs}(\lambda))/R_{rs}(560)$ becomes insensitive to changes in water properties. The reason for such a behavior can be traced back to the root of R_{rs}, which, based on the radiative transfer equation, is [14,15]

$$R_{rs} = G\frac{b_b}{a+b_b}, \tag{2}$$

where $G(\text{sr}^{-1})$ is a model parameter, with an average value $\sim 0.05\ \text{sr}^{-1}$ [16]; $b_b(\text{m}^{-1})$ is the backscattering coefficient of the bulk water, which includes the contribution of seawater (b_{bw}) and suspended particles (b_{bp}). For an easy illustration, let us consider that the model parameter G is independent for different waters; then $ip_{\text{Max-green}}$ can be expressed as

$$\frac{\text{Max}(R_{rs}(\lambda))}{R_{rs}(560)} \approx \frac{(b_b(\lambda))_{\text{Max}}}{b_b(560)}\frac{a(560)+b_b(560)}{(a(\lambda)+b_b(\lambda))_{\text{Max}}}, \tag{3}$$

where subscript "Max" indicates the wavelength corresponding to $\text{Max}(R_{rs}(\lambda))$. The absorption coefficient, an important inherent optical property (IOP), is the sum of the contributions of pure seawater (a_w), phytoplankton (a_{ph}), detritus (a_d), and gelbstoff (a_g); so the above ratio can be written as

$$\frac{\text{Max}(R_{rs}(\lambda))}{R_{rs}(560)} \approx \frac{(b_{bw}(\lambda)+b_{bp}(\lambda))_{\text{Max}}}{b_{bw}(560)+b_{bp}(560)}\frac{a_w(560)+a_{\text{ph}}(560)+a_{dg}(560)+b_{bw}(560)+b_{bp}(560)}{(a_w(\lambda)+a_{\text{ph}}(\lambda)+a_{dg}(\lambda)+b_{bw}(\lambda)+b_{bp}(\lambda))_{\text{Max}}}, \tag{4}$$

where a_d and a_g are combined as a_{dg}. The value of $a_w(560)$ is $0.062\ \text{m}^{-1}$ [17]. For waters with low concentrations of dissolved or suspended constituents, the contribution of $a_w(560)$ dominates the total absorption at 560 nm, while the contributions of other components at this wavelength are negligible. For instance, if [Chl] equals $1.0\ \text{mg}\,\text{m}^{-3}$, a value 10 times its global mode value [18], the corresponding $a_{\text{ph}}(560)$ is $\sim 0.007\ \text{m}^{-1}$ based on Bricaud *et al.* [19], and $a_{dg}(560)$ is even smaller for oceanic waters. In such cases, the ratio reflects

$$\frac{\text{Max}(R_{rs}(\lambda))}{R_{rs}(560)} \approx \frac{(b_{bw}(\lambda)+b_{bp}(\lambda))_{\text{Max}}}{b_{bw}(560)+b_{bp}(560)}\frac{a_w(560)}{(a_w(\lambda)+a_{\text{ph}}(\lambda)+a_{dg}(\lambda)+b_{bw}(\lambda)+b_{bp}(\lambda))_{\text{Max}}}. \tag{5}$$

Due to the small magnitude of b_{bp} for oceanic waters [20,21], b_{bp} will not contribute much to the above ratio [10]; thus, a change in $\text{Max}(R_{rs}(\lambda))/R_{rs}(560)$ reflects mainly changes in the total absorption coefficient corresponding to $\text{Max}(R_{rs}(\lambda))$. Basically, for such waters, $a_w(560)$ anchors the absorption coefficient at the longer wavelength of this ratio; so a or [Chl] can be estimated from such a ratio. For waters with high concentrations of dissolved or suspended constituents (e.g., when $a(440)$ becomes $\sim 1.0\ \text{m}^{-1}$ or higher), however, the contribution of a_w to total absorption at 560 nm becomes less important.

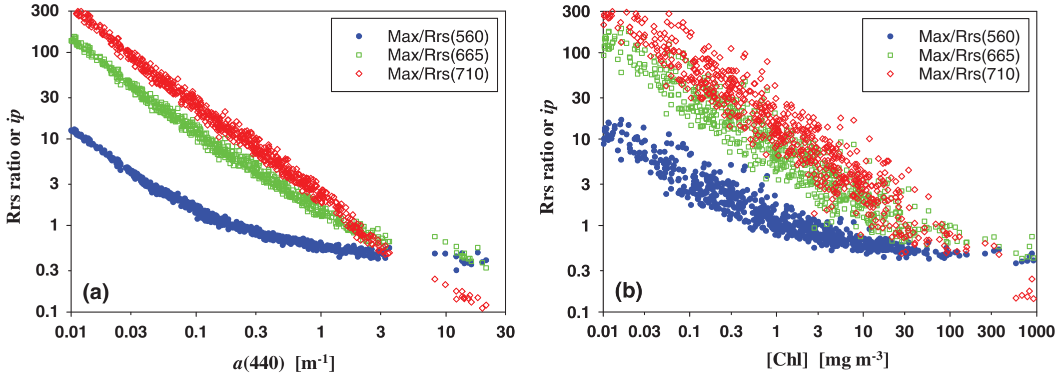

Fig. 1. Patterns among $a(440)$ (a), [Chl] (b), and R_{rs} ratios (*ip*) for large range of water properties. Data are from numerical simulations, where the scatters between [Chl] and *ip* are because there are multiple [Chl] for a given $a(440)$ [see Sections 2 and 4.C for details].

Also, because of the higher contribution of b_{bp} from the elevated particulates, b_{bw} becomes negligible. Eq. (4) then approximates

$$\frac{\mathrm{Max}(R_{rs}(\lambda))}{R_{rs}(560)} \approx \frac{(b_{bp}(\lambda))_{\mathrm{Max}}}{b_{bp}(560)} \frac{a_{\mathrm{ph}}(560) + a_{dg}(560) + b_{bp}(560)}{(a_{\mathrm{ph}}(\lambda) + a_{dg}(\lambda) + b_{bp}(\lambda))_{\mathrm{Max}}}. \tag{6}$$

In such a situation, there is no a_w to anchor the absorption coefficient at the green wavelength, and the magnitudes of the component absorption and backscattering coefficients to a large degree are cancelled out in the above ratio. Therefore, $\mathrm{Max}(R_{rs}(\lambda))/R_{rs}(560)$ plateaus for waters with high concentrations of constituents, which then loses sensitivity to a change in water properties.

Due to such limitations of the blue-green ratio, algorithms were developed to use ratios of R_{rs} in the red and/or infrared wavelengths for estimating [Chl] of turbid waters from water color [22–26]. Also, for waters with extremely high [Chl], or blooms, algorithms centered on the 710 nm band of MERIS were developed [27–29]. This requirement of different algorithms for waters with different concentrations (or turbidity) creates a challenge to produce seamless image products of water properties [5], where a hard-wired switch and/or a "bridge" have to be developed to connect clear and turbid waters in the same image [9,30,31]. To overcome such hard-wired switch and blending, Moore *et al.* [32] proposed an optical-water-type (OWT)-based scheme for [Chl] of coastal and lake waters. In such a scheme, a target R_{rs} spectrum has different weights of the designated OWTs, where either the OC4 algorithm or the red–infrared algorithm [24] is applied for initial estimate of [Chl], with the final [Chl] being a weighted average based on the weights of the associated OWTs [32].

Note that the separation of "clear" from "turbid" waters is quite subjective; thus, it is always a challenge to optimize the separation criterion and the blending. The fuzzy blending scheme of Moore *et al.* [32] avoided such hard-wired separation, but the mean R_{rs} spectra and the covariance matrix of the designated OWTs are dependent on water-type resolution (number of water types), R_{rs} data, and/or regions [32]. In addition, the application of such a fuzzy-logic-based scheme is not as straightforward as the explicit algorithms of OC4 type.

To maintain the spatial variability included in the original ocean color image, it is always desired to use one algorithm, instead of multiple algorithms, to process satellite ocean color data [5]. Therefore, in this study, using the MERIS band setting as an example, we propose an innovative progressive blending scheme that can seamlessly produce a large dynamic range of a or [Chl], a range effectively covering waters from oceanic gyres to extremely turbid coastal/inland waters. An application of such an algorithm to ocean color images in the coastal zone can then produce spatially seamless bio-optical properties, as demonstrated in a later part of this article.

2. DATA

Two datasets are used in this effort. 1) *Simulated*: a dataset of wide range of inherent (IOPs) and apparent (AOPs) optical properties simulated by Hydrolight [33]; 2) *Measured*: A dataset of bio-optical properties collected in various regions of the world, which includes those data collected in the Chinese seas and coastal waters and those compiled from searching the SeaWiFS Bio-optical Archive and Storage System (SeaBASS). Since details of the two datasets were well described in other articles [34,35], they are briefly summarized here. To provide a general picture of the dynamic range of water properties of these datasets, Fig. 2 presents a histogram of $a(440)$ of both datasets, where the two have generally similar distributions, with more values centered in the range of ~0.1–1.0 m^{-1}.

Simulated: This dataset has hyperspectral (350–800 nm, 5 nm step) a_{ph} spectra measured worldwide, along with other IOPs varying with $a_{\mathrm{ph}}(440)$ but in a constrained range. The sun was set at 30° from zenith under a clear sky, and inelastic contributions from Raman scattering and chlorophyll-a fluorescence were included. Details of the IOPs setup and simulations can be found in Lee *et al.* [34]. The resulted $a(440)$ ranged ~0.008–100 m^{-1}, but here only the range of ~0.008–20.0 m^{-1} (674 data points) is used. Waters with $a(440)$ higher than 20.0 m^{-1} is rare in natural environment; also, passive remote sensing may not be suitable for waters with an absorption coefficient higher than 20.0 m^{-1}. Because it is simulated based on radiative transfer, this dataset can be considered as free of measurement errors or uncertainties.

Measured: This dataset includes R_{rs} and IOPs from field measurements. The data (of 573 stations) from Chinese seas and coastal waters were compiled from a total of 40 cruises during 2003–2015 in the regions of Xiamen Bay, the Taiwan Strait, the South China Sea, the Changjiang River, the Jiulongjiang River, etc. R_{rs} of these data were measured with a handheld spectrometer covering a spectral range of ~350–1100 nm (resolution being ~3 nm), where the radiance from water, sky, and a standard plaque were measured. R_{rs} spectrum was then calculated from these measurements following Lee *et al.* [36]. Using MERIS as an example for this study, R_{rs} values at 412 nm, 443 nm, 489 nm, 510 nm, 560 nm, 665 nm, and 710 nm were used for this effort. The total absorption coefficient was calculated as the sum of a_w, a_{ph}, a_d and a_g. Values of the non-water components and chlorophyll concentration were obtained from measurements of water samples in the surface layer. Details of such measurements were described in Shang *et al.* [37]. For the 573 sets of R_{rs} versus $a(440)$, $a(490)$, or [Chl], $a(440)$ is in a range of ~0.01–14.0 m^{-1} and [Chl], ~0.03–130.0 $\mathrm{mg\,m}^{-3}$.

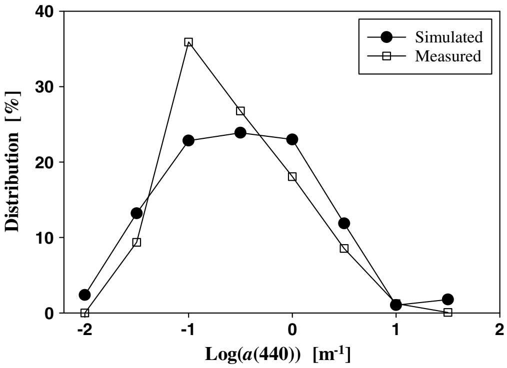

Fig. 2. Histograms of $a(440)$ of simulated and measured datasets, respectively. Due to the wide dynamic range, the histogram is presented for $a(440)$ in log-base 10.

Also included in the *Measured* dataset are R_{rs}, [Chl], a_{ph}, a_d, and a_g by searching SeaBASS. As in Werdell and Bailey [38], the total absorption coefficient was calculated as the sum of a_w, a_{ph}, a_d, and a_g. There are few data with R_{rs} at 710 nm, so for this subset the wavelengths of R_{rs} are 412 nm, 443 nm, 489 nm, 510 nm, 560 nm, and 665 nm, and about 1000 pairs of R_{rs} versus $a(440)$ and $a(490)$ were compiled, while about 4000 pairs of R_{rs} versus [Chl] were compiled.

3. PROGRESSIVE EMPIRICAL ALGORITHM

A. Overall Scheme for Algorithm Input

Following Eqs. (4)–(6), in order to have a ratio-based *ip* that is sensitive to the large range of absorption coefficients in the blue wavelengths, it is important to have a_w of the band in the denominator (longer wavelength) of the R_{rs} ratio making significant contributions to the total absorption coefficient. Basically, this requirement anchors the denominator of the ratio, which will result in changes in $\mathrm{Max}(R_{rs}(\lambda))/R_{rs}$(longer wavelength) being driven mainly by the change in absorption coefficient corresponding to $\mathrm{Max}(R_{rs}(\lambda))$. This feature is highlighted by the ratios of $\mathrm{Max}(R_{rs}(\lambda))/R_{rs}(665)$ and $\mathrm{Max}(R_{rs}(\lambda))/R_{rs}(710)$, which are also included in Fig. 1, with data from the *Simulated* dataset. Because $a_w(665) = 0.43\ \mathrm{m}^{-1}$ and $a_w(710) = 0.83\ \mathrm{m}^{-1}$ [17], the slope (in log scale) of $\mathrm{Max}(R_{rs}(\lambda))/R_{rs}(710)$ does not vary much when $a(440)$ is varied for more than four orders of magnitude, while the slope of $\mathrm{Max}(R_{rs}(\lambda))/R_{rs}(665)$ becomes smaller when $a(440)$ is greater than $\sim 5.0\ \mathrm{m}^{-1}$. The stable slope of $\mathrm{Max}(R_{rs}(\lambda))/R_{rs}(710)$ indicates that this ratio is sensitive for a wide range of $a(440)$, which shows the advantage of using R_{rs} in the longer wavelength as the anchor of R_{rs} ratio in estimating water properties. However, because $R_{rs}(710)$ value is extremely low in oceanic waters, it is nearly impossible to get an accurate $R_{rs}(710)$ product from a satellite ocean color sensor; thus, this use of $R_{rs}(710)$ as the denominator has to be restricted to turbid waters where $R_{rs}(710)$ value is high.

From these observations, it is imperative to progressively incorporate R_{rs} from green to red (or infrared) as the anchor in such a ratio in order to generate water properties for an image including both clear and turbid waters. We thus, after various trial-and-error tests, propose the following ratio (with MERIS band as an example) from R_{rs} as the *ip* (termed as $ip_{\text{Max-Sum}}$) for empirical algorithms aimed at [Chl] or the absorption coefficient:

$$ip_{\text{Max-Sum}} = \frac{\mathrm{Max}(R_{rs}(440), R_{rs}(490), R_{rs}(510))}{Sum(R_{rs}(560), p_1 \times R_{rs}(665), p_2 \times R_{rs}(710))}, \tag{7}$$

where p_1 and p_2 are empirical scaling parameters to increase the weights of $R_{rs}(665)$ and $R_{rs}(710)$ in such a ratio or empirical algorithms. After parameters of p_1 and p_2 are determined, the above formula will progressively use $R_{rs}(560)$, $R_{rs}(665)$, and $R_{rs}(710)$ in the denominator for estimating [Chl] or the absorption coefficient. Through this change in input parameter from $ip_{\text{Max-green}}$ to $ip_{\text{Max-Sum}}$, an algorithm can then seamlessly cover waters from oceanic to turbid coastal waters with one formula. Analogous to BGRA, we term this type of algorithm as max-sum-ratio algorithm (MSRA) to highlight the progressive utilization of R_{rs} in the blue to red (or even longer) wavelengths for water properties. For SeaWiFS, MODIS, and VIIRS having no spectral band at 710 nm, likely the band around 750 nm has to be used for highly turbid waters [22,24], which will require dedicated efforts to ensure the accuracy of R_{rs} at such a band.

B. Determination of Scaling Parameters

The values of p_1 and p_2 cannot be set too low or too high. When they are set too low, the contributions of $R_{rs}(665)$ and $R_{rs}(710)$ to the denominator will be small, limiting its contribution to the sensitivity of MSRA for highly turbid waters. On the other hand, if their values are set too high, they may amplify questionable $R_{rs}(665)$ or $R_{rs}(710)$ when their values are very low (for oceanic waters). Therefore, an optimized setting is necessary for p_1 and p_2.

For this optimization, rather than setting parameters p_1 and p_2 to global constants, we allow them to change dynamically with water properties, and this change is represented using the ratio of $R_{rs}(665)/R_{rs}(490)$ (for p_1) and $R_{rs}(710)/R_{rs}(490)$ (for p_2). Values of these two ratios are small for oceanic waters, so $R_{rs}(665)$ and $R_{rs}(710)$ do not contribute much to the denominator of $ip_{\text{Max-Sum}}$ in such cases. However, values of the two ratios are high for coastal turbid waters; then, $R_{rs}(665)$ and $R_{rs}(710)$ play progressively bigger roles in $ip_{\text{Max-Sum}}$ for coastal turbid waters. Empirically, p_1 and p_2 are modeled as follows:

$$p_1 = x_1 \left(\frac{R_{rs}(665)}{R_{rs}(490)}\right)^{x_2}, \quad p_2 = y_1 \left(\frac{R_{rs}(710)}{R_{rs}(490)}\right)^{y_2}. \tag{8}$$

Values of $x_{1,2}$ and $y_{1,2}$ were subsequently derived through best fitting between $\log(ip_{\text{Max-Sum}})$ and $\log[a(440)]$, and this best fitting is measured by the highest coefficient of determination (R^2) in a linear relationship between $\log(ip_{\text{Max-Sum}})$ and $\log[a(440)]$. The data used for this determination are from the *Simulated* dataset. Table 1 presents the obtained $x_{1,2}$ and $y_{1,2}$ values. For the $a(440)$ range, the R^2 value is 0.99 between $\log[a(440)]$ and $\log(ip_{\text{Max-Sum}})$, but 0.88 between $\log[a(440)]$ and $\log(\mathrm{Max}(R_{rs}(\lambda))/R_{rs}(560))$, indicating a much higher predictability of $ip_{\text{Max-Sum}}$. Figure 3 presents the ranges and variations of p_1 and p_2, which show the weighting factors applied to $R_{rs}(665)$ and $R_{rs}(710)$, respectively, compared to $R_{rs}(560)$ when $ip_{\text{Max-Sum}}$ is calculated. For example, p_1 is higher than ~ 3.0 when $a(440)$ becomes $\sim 1.0\ \mathrm{m}^{-1}$, and p_2 is higher than 1.0 when $a(440)$ becomes $\sim 3.0\ \mathrm{m}^{-1}$, which amplifies the roles of $R_{rs}(665)$ and $R_{rs}(710)$ in the calculation of $ip_{\text{Max-Sum}}$ for turbid waters. On the other hand, p_1 is just about 1.5, and p_2 is less than 0.01 for $a(440) < 0.03\ \mathrm{m}^{-1}$, which significantly limits the contributions of $R_{rs}(665)$ and $R_{rs}(710)$ to $ip_{\text{Max-Sum}}$ for oceanic waters.

To highlight the improved sensitivity of $ip_{\text{Max-Sum}}$ to changes in $a(440)$, the relative change in *ip* (rc_{ip}) for a change in $a(440)$ is calculated as

Table 1. Empirical Coefficients for Parameters to Scale R_{rs} for Algorithm $ip_{\text{Max-Sum}}$

x_1	x_2	y_1	y_2
4.0	0.27	0.65	0.94

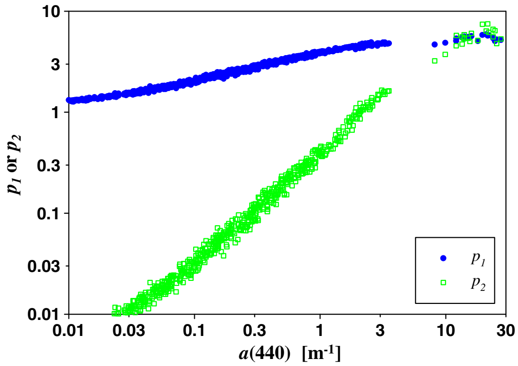

Fig. 3. Variation of p_1 and p_2 for a wide range of $a(440)$.

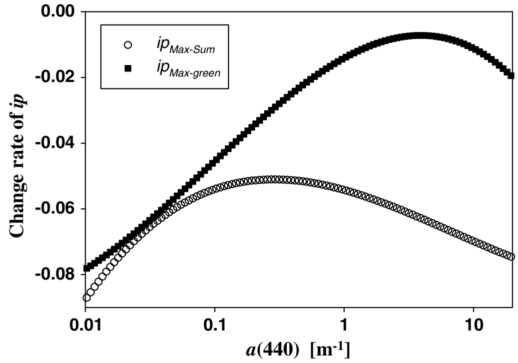

Fig. 4. Relative change (rc_{ip}) of the two ip, respectively, for a wide range of $a(440)$.

$$rc_{ip} = 2\frac{ip(a_2) - ip(a_1)}{ip(a_2) + ip(a_1)}, \tag{9}$$

where a_1 and a_2 represent two $a(440)$ values, and $a_2 > a_1$. This rc_{ip} basically represents a normalized change in ip for changes in $a(440)$. The greater the absolute value of rc_{ip}, the higher the sensitivity of ip to the change in $a(440)$; if rc_{ip} is 0, it shows an ip is insensitive to the change in $a(440)$. The "normalization" is to keep the change in ip comparable, as the absolute values of $ip_{\text{Max-green}}$ and $ip_{\text{Max-Sum}}$ are quite different due to the different math formulas used. Figure 4 compares rc_{ip} for $ip_{\text{Max-Sum}}$ and that for $ip_{\text{Max-green}}$, where the negative rc_{ip} values show that ip decreases with increasing $a(440)$. The absolute value of rc_{ip} for $ip_{\text{Max-Sum}}$ is about 0.06–0.08 for $a(440) > 1.0\ \text{m}^{-1}$ (equivalent [Chl] is ~10.0 mg m^{-3}), which is about five times greater than the absolute rc_{ip} value for $ip_{\text{Max-green}}$. This comparison indicates the significantly improved sensitivity of $ip_{\text{Max-Sum}}$ to change in the absorption coefficient in turbid waters.

4. EMPIRICAL ALGORITHMS FOR ABSORPTION COEFFICIENTS AND CHLOROPHYLL CONCENTRATION

A. *a*(440)

With the optimized formula of $ip_{\text{Max-Sum}}$, and taking the conventional approach of polynomial fitting [5] for an empirical algorithm, a simple empirical algorithm for estimating $a(440)$ can be written as follows:

$$\begin{aligned}&\log(a(440) - a_w(440))\\&= \alpha_0 + \alpha_1 \times x + \alpha_2 \times x^2 + \alpha_3 \times x^3 + \alpha_4 \times x^4,\end{aligned} \tag{10}$$

where $x = \log(ip_{\text{Max-Sum}})$. Values of α_{0-4}, derived by fitting simulated and measured data, respectively, are presented in Table 2. The fitting tool used is the generalized reduced gradient (GRG) algorithm embedded in Microsoft Excel Solver. Figure 5(a) shows the modeled $a(440)$ compared with $a(440)$ of the *Simulated* dataset. For $a(440)$ in a range of ~0.008–20.0 m^{-1}, the mean absolute percent difference (MAPD) between the two is ~8% (see Table 3), with MAPD calculated as follows:

$$\text{MAPD} = \frac{1}{N}\sum_{N}\frac{|P^{\text{est}} - P^{\text{known}}|}{P^{\text{known}}} \times 100, \tag{11}$$

where P represents a desired water property, and P^{est} is for that property obtained from an algorithm, while P^{known} is from either simulations or measurements. Also included in Tables 3 and 4 are the R^2 values between known (or measured) and estimated properties in linear and log scales, respectively. The root-mean-square-difference in log scale ($\text{RMSD}_{\log}$) is calculated as follows:

$$\text{RMSD}_{\log} = \sqrt{\frac{1}{N}\sum_{N}(\log(P^{\text{known}}) - \log(P^{\text{est}}))^2}. \tag{12}$$

Figure 5(b) shows how estimated $a(440)$ using the above empirical algorithm compares with $a(440)$ for the *Measured* dataset ($a(440)$ in a range of ~0.01–14.0 m^{-1}), along with the performance measure presented in Table 4. Note that there was no change in algorithm coefficients when Eq. (10) was

Table 2. Algorithm Coefficients with $ip_{\text{Max-Sum}}$ as the Input for Absorption Coefficients and [Chl][a]

	Property	α_0	α_1	α_2	α_3	α_4
Simulated data	$a(440)$	−0.9031	−1.3299	0.0214	0.0402	−0.0233
	$a(560)$	−1.6625	−1.3794	0.0234	−0.0367	−0.0283
	$a_{\text{ph}}(440)$	−1.5394	−1.1957	0.2896	−0.0871	−0.0859
	[Chl]	−0.1589	−1.7686	0.1410	−0.0647	−0.0329
Measured data	$a_{\text{ph}}(440)$	−1.3056	−1.0252	0.308	−0.3651	−0.1838
	[Chl]	0.0351	−1.4663	−0.070	0	0

[a] The upper four rows are for algorithm coefficients developed based on the *Simulated* dataset, while the lower two rows are for algorithm coefficients developed based on the *Measured* dataset.

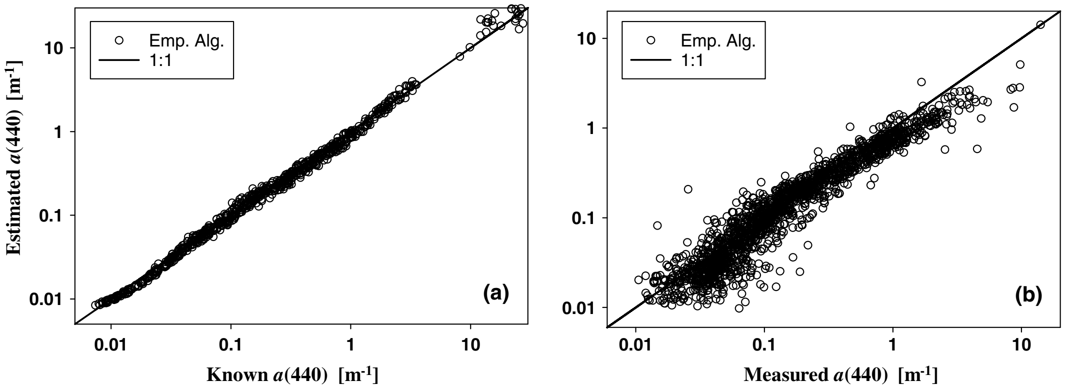

Fig. 5. Scatter plot between known and empirically estimated $a(440)$ from $ip_{\text{Max-Sum}}$: *Simulated* dataset (a), and *Measured* dataset (b).

Table 3. Statistical Measure of Algorithm Performance for the Simulated Data

	Property	MAPD	R^2	$\text{RMSD}_{\log}$	Int. in Log Scale	R^2 (in log scale)	N
Emp.	$a(440)$	0.08	0.98	0.05	−0.013	0.995	674
	$a_{\text{ph}}(440)$	0.21	0.93	0.11	−0.009	0.978	674
	[Chl]	0.60	0.57	0.29	0.009	0.931	674
QAA	$a(440)$	0.11	0.96	0.06	0.090	0.99	674
	$a(490)$	0.08	0.97	0.05	0.071	0.99	674
	$a(560)$	0.06	0.97	0.04	−0.013	0.98	674

Table 4. Statistical Measure of Algorithm Performance for the Measured Data

	Property	MAPD	R^2	$\text{RMSD}_{\log}$	Int. in Log Scale	R^2 (in log scale)	N
Emp.	$a(440)$	0.28	0.77	0.19	−0.094	0.91	1667
	$a_{\text{ph}}(440)$	0.53	0.56	0.32	−0.353	0.84	1781
	[Chl]	0.76	0.21	0.37	−0.186	0.82	4448
QAA	$a(440)$	0.28	0.64	0.19	−0.174	0.91	1667
	$a(490)$	0.24	0.64	0.16	−0.165	0.92	1666
	$a(560)$	0.11	0.73	0.08	−0.192	0.91	1643

applied to this *Measured* dataset, but the estimated $a(440)$ values from $ip_{\text{Max-Sum}}$ are generally scattered around the 1:1 line, with R^2 and MAPD values of 0.77 and ∼28%, respectively. These values indicate a general consistency of R_{rs} versus absorption coefficient between the *Simulated* and *Measured* datasets. The lower R^2 and higher MAPD values found in the *Measured* dataset are due to a wide range of uncertainties associated with the measurements of R_{rs} and a, and/or spatial mismatches between R_{rs} and a during field measurements.

B. $a_{\text{ph}}(440)$

In a similar fashion for $a(440)$, replacing $a(440) - a_w(440)$ in Eq. (10) with $a_{\text{ph}}(440)$, a polynomial-type algorithm for $a_{\text{ph}}(440)$ can be developed using $ip_{\text{Max-Sum}}$ as the input parameter, with the algorithm coefficients included in Table 2. Figure 6 shows known (or measured) $a_{\text{ph}}(440)$ compared with estimated $a_{\text{ph}}(440)$, for both *Simulated* and *Measured* datasets. Compared to the results of $a(440)$, the R^2 values between $ip_{\text{Max-Sum}}$ and $a_{\text{ph}}(440)$ are reduced (see Tables 3 and 4), while the MAPD and RMSD values are increased, for both *Simulated* and *Measured* data. This is not a surprise because R_{rs} is determined by the total absorption coefficient [see Eqs. (1) and (3), for instance], not by an individual component; so there is more scattering, or less predictability, between $a_{\text{ph}}(440)$ and $ip_{\text{Max-Sum}}$.

Further, when the same set of algorithm coefficients for $a_{\text{ph}}(440)$ developed from the *Simulated* dataset is applied to the *Measured* dataset, the derived $a_{\text{ph}}(440)$ values from $ip_{\text{Max-Sum}}$ are generally lower than the measured values, whereas no such systematic bias was discovered for $a(440)$. This is also represented by the negative bias for $a_{\text{ph}}(440)$ of the *Measured* dataset (see Table 4). This is likely due to the fact that the relative contribution of a_{ph} to the total absorption in the *Simulated* dataset is lower than the average relative contribution of natural waters (or for this dataset obtained from field measurements); thus, the $a_{\text{ph}}(440)$ from the empirical algorithm tuned based on the *Simulated* dataset shows a lower bias with the *Measured* dataset. Fundamentally, this is because $ip_{\text{Max-Sum}}$ represents the total absorption coefficient, rather than the contribution of an individual component. To overcome this

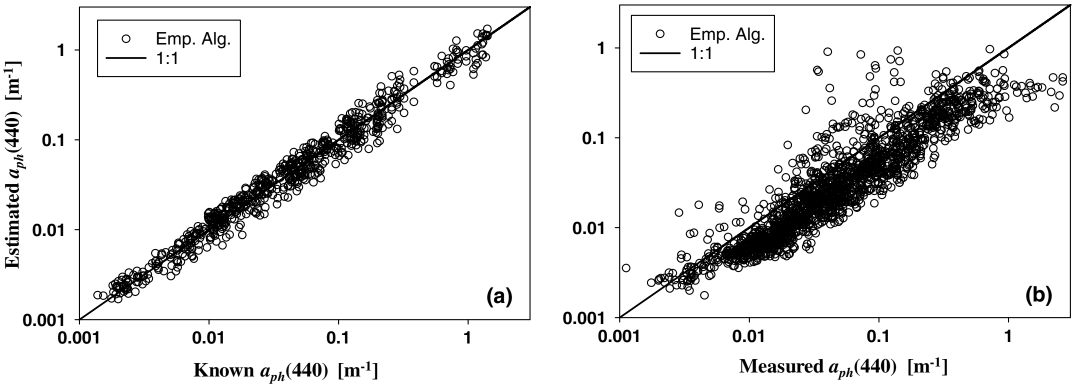

Fig. 6. Same as Fig. 5, except for $a_{\mathrm{ph}}(440)$.

bias, another set of algorithm coefficients (see Table 2) was derived using $a_{\mathrm{ph}}(440)$ and $ip_{\text{Max-Sum}}$ from the *Measured* dataset. However, since such empirical algorithms aimed for one contributing component are inherently data dependent, its applicability to other regions is always subjective to the natural variability of the bio-optical properties of the targeted region [39].

C. [Chl]

Since [Chl] is of great interest for marine biology and ecosystem status, we used the same approach for $a_{\mathrm{ph}}(440)$ to estimate [Chl] from $ip_{\text{Max-Sum}}$. First, we converted $a_{\mathrm{ph}}(440)$ to [Chl] for the *Simulated* dataset; this conversion is determined by the chlorophyll-specific absorption coefficient ($a^*_{\mathrm{ph}}(440)$, $\mathrm{m}^2\ \mathrm{mg}^{-1}$). As shown in numerous studies [19,40], there is no constant or one-to-one relationship between $a^*_{\mathrm{ph}}(440)$ and [Chl]; rather, there are multiple $a^*_{\mathrm{ph}}(440)$ for a given [Chl]. To represent this observation found in the field, following Bricaud *et al.* [19,41], $a^*_{\mathrm{ph}}(440)$ is modeled as follows:

$$a^*_{\mathrm{ph}}(440) = A([\mathrm{Chl}])^{B-1}. \tag{13}$$

In (13), A and B are constrained random values:

$$A = 0.02 + 0.04\ \mathrm{rand}, \tag{14a}$$

$$B = 0.55 + 0.2\ \mathrm{rand}, \tag{14b}$$

where rand represents a random value (in the range of 0–1) generator. Figure 7 compares the modeled $a^*_{\mathrm{ph}}(440)$ of the *Simulated* dataset using the statistical relationship showing in Bricaud *et al.* [19], where a general consistency is achieved. [Chl] of the *Simulated* dataset is then obtained as the ratio of $a_{\mathrm{ph}}(440)$ to $a^*_{\mathrm{ph}}(440)$.

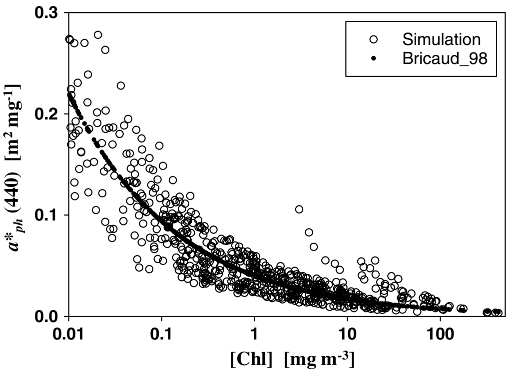

Fig. 7. Relationship between $a^*_{\mathrm{ph}}(440)$ and [Chl].

Taking the same approach for $a_{\mathrm{ph}}(440)$, an empirical algorithm for [Chl] with $ip_{\text{Max-Sum}}$ as the ip is also developed, and the algorithm coefficients and statistical performance are included in Tables 2–4. Figure 8 compares known [Chl] with algorithm-estimated [Chl]. Not surprisingly, the performance of [Chl] algorithm is further deteriorated compared to $a(440)$ or $a_{\mathrm{ph}}(440)$, for both *Simulated* and *Measured* datasets. In particular, as would be expected and pointed out before [12,42], due to the variation in $a^*_{\mathrm{ph}}(440)$, the statistical results for [Chl] are worse than those for $a_{\mathrm{ph}}(440)$.

D. Extension to QAA

QAA stands for the quasi-analytical algorithm, which was developed to semi-analytically invert R_{rs} to obtain waters' IOPs [43]. It takes a step-wise fashion to retrieve IOPs. An important first step is to estimate the absorption coefficient at a reference wavelength [$a(\lambda_0)$]. In the latest version (v6) of QAA, $a(\lambda_0)$ is set around 550 nm for oceanic waters and around 670 nm for turbid waters. It then runs into the same dilemma to connect results of clear and turbid waters. Following the above practices, we use $ip_{\text{Max-Sum}}$ to estimate $a(\lambda_0)$ for "all" waters, thus avoiding the arbitrary switching and then bridging of results using $a(\lambda_0)$ of clear and turbid waters. As $a(440)$, an empirical algorithm for $a(560)$ using $ip_{\text{Max-Sum}}$ as the input is developed, and the algorithm coefficients are included in Table 2. Subsequently, by implementing the other steps of QAA, values of $a(440)$ are retrieved analytically from R_{rs}. Figures 9 and 10 show the derived $a(440)$ and $a(490)$ compared with known or measured values, respectively. Statistical measures of the performance are included in Tables 3 and 4. The overall average percent difference is ~11% for $a(440)$ and ~8% for $a(490)$ for the *Simulated* dataset, indicating robust inversion results. There is a slight overestimate at the higher end (for $a(440) > {\sim}2.0\,\mathrm{m}^{-1}$), which is a result of the impact of imperfect estimate of the power-law parameter related to the spectral dependence of $b_{bp}(\lambda)$ [10], which is still a challenge to accurately estimate this spectral dependence [44]. On the other hand, the results show that, through such an analytical scheme, one empirical function for $a(\lambda_0)$ is sufficient to

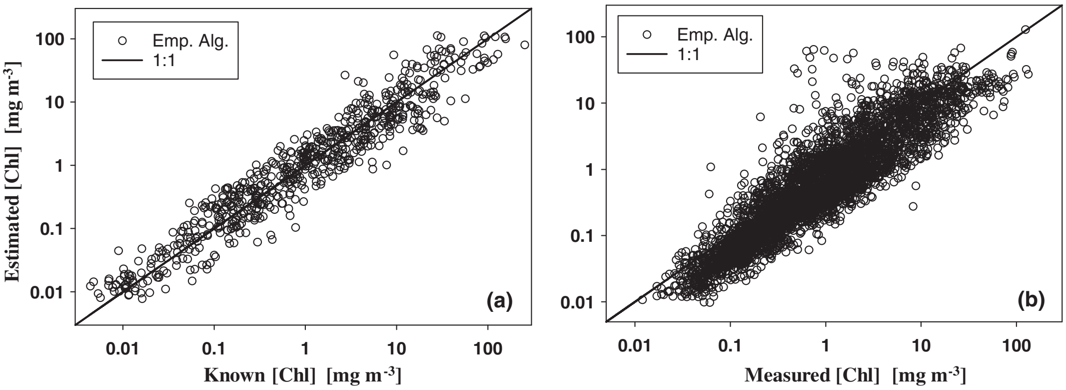

Fig. 8. Same as Fig. 5, except for [Chl].

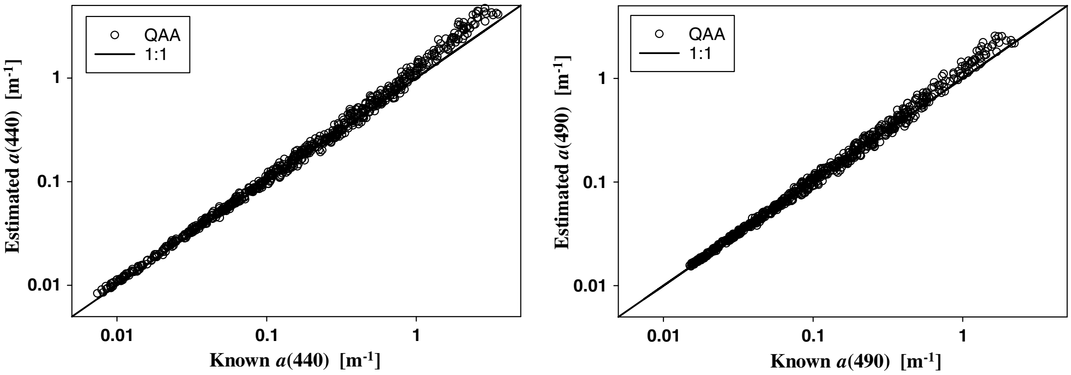

Fig. 9. Scatter plot between known and QAA-derived estimated total absorption coefficient of the *Simulated* dataset. (left) For $a(440)$; (right) for $a(490)$.

obtain absorption coefficients of multiple wavelengths, rather than multiple sets of empirical coefficients for each desired wavelength.

E. Examples with MERIS Data

To demonstrate the application of MSRA with ocean color images, the algorithm with $ip_{\text{Max-Sum}}$ developed for $a(440)$ was applied to two sample MERIS images (Fig. 11). One is a region in the vicinity of the Changjiang River estuary, while the other is a region near Monterey Bay, CA; both locations experience strong interactions of oceanic and turbid coastal waters. For the water near the Changjiang River estuary, $a(440)$ increased from ~0.02 m^{-1} in the East China Sea to ~2.0 m^{-1} near the mouth of the Changjiang River, covering three orders of magnitude. For the region of Monterey Bay, $a(440)$ varied from ~0.1 m^{-1} to ~2.0 m^{-1}, also indicating a highly dynamic environment. Although there are no concurrent matchup *in situ* data to validate these satellite products, which is beyond the scope of this effort, these patterns are consistent with historical observations [45].

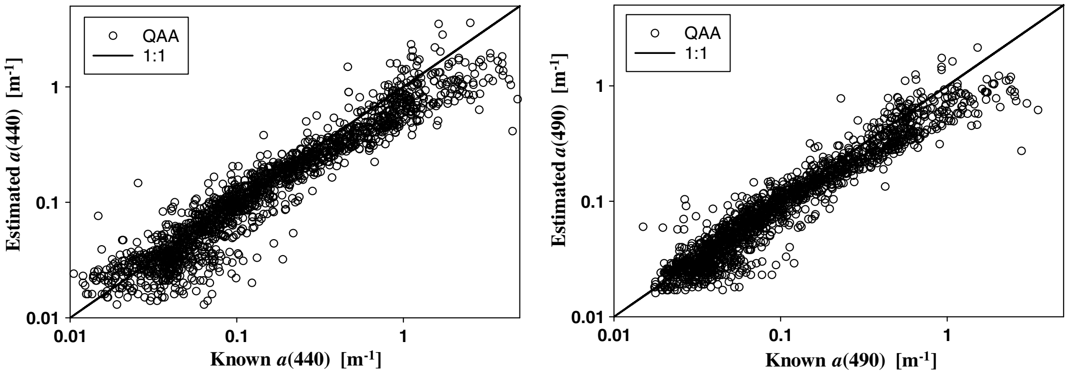

Fig. 10. Same as Fig. 9, but for the *Measured* dataset.

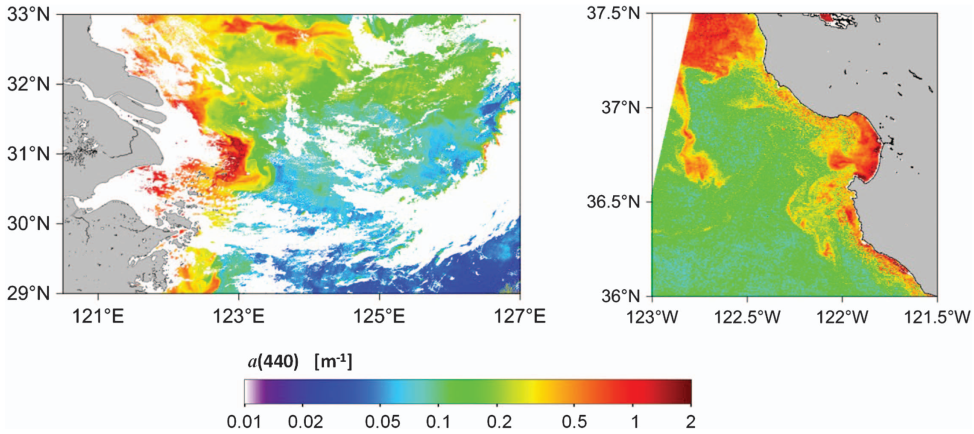

Fig. 11. An application of $ip_{\text{Max-Sum}}$-based $a(440)$ algorithm to images obtained by MERIS. (left) Changjiang River estuary and the East China Sea on 9 September 2008; (right) Monterey Bay and eastern Pacific Ocean on 27 October 2006. Gray color indicates land, and white color indicates no R_{rs} data due to cloud or failed atmospheric correction.

To indicate the progressive roles of $R_{rs}(665)$ and $R_{rs}(710)$ in MSRA when processing ocean color images, Fig. 12 shows the ratios of $p_1^*R_{rs}(665)/R_{rs}(560)$ and $p_2^*R_{rs}(710)/R_{rs}(560)$, as they indicate the locations where $p_1^*R_{rs}(665)$ and $p_2^*R_{rs}(710)$ start to play more significant roles compared to $R_{rs}(560)$ in MSRA. For the image of Changjiang River estuary, $p_1^*R_{rs}(665)/R_{rs}(560)$ and $p_2^*R_{rs}(710)/R_{rs}(560)$ are generally less than ~0.3 offshore, which indicates $R_{rs}(560)$ plays a major role in the denominator of MSRA for these waters. These ratios gradually increase towards inshore, with $p_1^*R_{rs}(665)/R_{rs}(560)$ and $p_2^*R_{rs}(710)/R_{rs}(560)$ as high as ~3 at the river mouth, thus progressively $R_{rs}(665)$ and $R_{rs}(710)$ play bigger and bigger roles for such turbid waters. The same kind of patterns also appear for the image of Monterey Bay, where $p_1^*R_{rs}(665)/R_{rs}(560)$ and $p_2^*R_{rs}(710)/R_{rs}(560)$ are generally less than ~0.5 and 0.1, respectively, for offshore waters, but increase to ~2 for waters near the coast. Therefore $R_{rs}(665)$ and $R_{rs}(710)$ progressively play bigger roles when processing an ocean color image covering both oceanic and coastal waters rather than to make a hard-wired switch for some of the pixels in an image. This is especially so for the patch of waters showing phytoplankton bloom offshore Monterey Bay, where values of $R_{rs}(710)$ are significantly higher than surrounding waters.

Note that only image products of $a(440)$ are presented here. This is because $a(440)$, $a_{\text{ph}}(440)$, and [Chl] are all produced with the same $ip_{\text{Max-Sum}}$, although with different coefficients for their empirical algorithms; thus, the spatial patterns of these three products are the same from an ocean color satellite

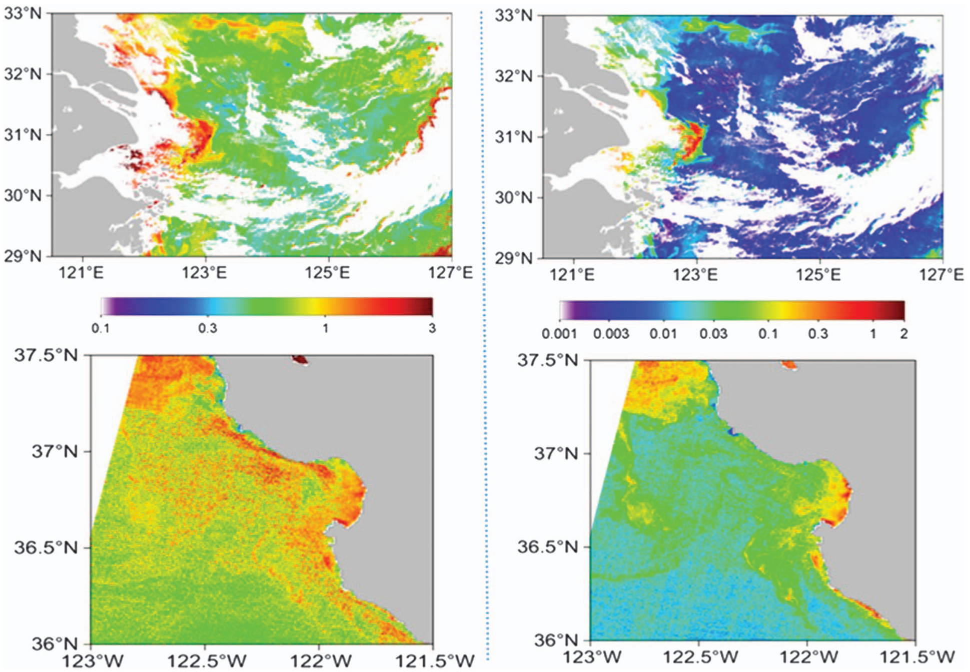

Fig. 12. Ratios of $p_1^*R_{rs}(665)/R_{rs}(560)$ (left) and $p_2^*R_{rs}(710)/R_{rs}(560)$ (right) for the absorption coefficient images in Fig. 11. (Top panel) Changjiang River estuary; (bottom panel) Monterey Bay.

image. This also highlights the inherent limitations of such empirical algorithms for "multiple" water properties, where, for instance, the image products of [Chl] and $K_d(490)$ generated by the standard (or default) ocean color algorithms (https://earthdata.nasa.gov/) have nearly identical spatial patterns. In other words, although for a given pixel the value of $K_d(490)$ is different from the value of [Chl], the $K_d(490)$ image product does not provide new spatial information.

5. DISCUSSION AND CONCLUSION

As presented in previous studies [13,25,46], using either simple color ratios or semi-analytical algorithms, the inclusion of R_{rs} information in the longer wavelengths is important for the retrieval of water properties of more turbid waters. For atmospheric correction, this wavelength might be in the near-infrared or shortwave range to ensure no contribution from waters in the measured total radiance [47]. For the retrieval of water properties from R_{rs} spectrum, an algorithm should include R_{rs}information in the red/near-infrared or even longer wavelengths [48], as only in these wavelengths is there a known property, a_w, to constrain R_{rs} with one variable (b_{bp}), rather than two variables [b_{bp} and a, see Eq. (2)]. To minimize or avoid ambiguities encountered in conventional blue–green R_{rs} ratios, or to increase the sensitivity of R_{rs} ratios to change in water properties, it is necessary and important to include R_{rs} in the longer wavelength in such ratios. This requirement also demands further improvement in R_{rs} quality in the longer wavelengths [47,49].

Nevertheless, the $ip_{\text{Max-Sum}}$ developed here is still a ratio of R_{rs} at different bands. Because R_{rs} represents the ratio of $b_b/(a + b_b)$, change in such R_{rs} ratios is still the best at representing change in the total absorption coefficient after considering the contribution of b_b is relatively small. The total absorption coefficient is a sum of a_w, a_{ph}, a_d, and a_g, and chlorophyll-a is just one of the many pigments contributing to a_{ph}; thus, this change in R_{rs} ratio does not necessarily represent change in [Chl], unless it is case-1 water where all optical properties co-vary with [Chl] [6,8]. But, oceanic waters are not necessarily case-1 [50,51], as this definition is not based on locations or regions, rather it is based on the dependence between IOPs and [Chl]. Therefore, we should always keep in mind that R_{rs}-ratio derived [Chl] from satellite images represents the best spatial distribution of the total absorption coefficient in general, where higher values likely represent higher [Chl], a phenomenon of the natural environment. And from such R_{rs}-ratio algorithms, uncertainties increase from the retrieved $a(440)$, to $a_{\text{ph}}(440)$, and then to [Chl].

Here, through innovative and dynamic inclusion of R_{rs} in the red–infrared bands in the R_{rs} ratio ($ip_{\text{Max-Sum}}$), the sensitivity of $ip_{\text{Max-Sum}}$ is significantly increased for more turbid waters than that of the conventional $ip_{\text{Max-green}}$. Therefore, one empirical formula or algorithm for a or [Chl] can be applied to waters from oceanic gyres to turbid coastal waters, which avoids a hard-wired arbitrary switch of two algorithms developed separately for clear and turbid waters. Such a scheme is also easier to implement than the OWT-based fuzzy-logic approach [32]. Further, extending this scheme to the widely used QAA, a high dynamic range of the total absorption coefficient [$a(440)$ in a range of $\sim$0.01–20.0 m^{-1}] can be derived from R_{rs} spectrum without a switch of the reference wavelength. Although its application was demonstrated only with MERIS images, it is envisioned that such a scheme can be applied to other ocean color satellite data after slight modifications based on the sensor's band specifics. However, for the evaluation or validation of such R_{rs} inversion (empirical or semi-analytical), one of the biggest challenges is to reduce measurement uncertainties. These uncertainties can be larger than those caused by algorithms (at least for the total absorption coefficient); thus, it is difficult to isolate algorithm deficiency when there are gaps between R_{rs} inversion and measured values.

Funding. The National Key Research and Development Program of China, Ministry of Science and Technology of the People's Republic of China (MOST) (2016YFC1400906, 2018YFC1407504); National Natural Science Foundation of China (NSFC) (41576169, 41776184); National Oceanic and Atmospheric Administration (NOAA) (NA11OAR4320199); University of Massachusetts Boston.

Acknowledgment. We are grateful to all colleagues who provided data to the SeaBASS. Comments and suggestions from three anonymous reviewers greatly improved the manuscript. This paper is Contribution No. 2019335 of the State Key Laboratory of Marine Environmental Science, Xiamen University.

Shang acknowledges funding from The National Key Research and Development Program of China, Ministry of Science and Technology of the People's Republic of China (MOST), and the National Natural Science Foundation of China (NSFC); Lee acknowledges funding from the National Oceanic and Atmospheric Admininstration (NOAA), and the University of Massachusetts Boston.

REFERENCES

1. W. W. Gregg, N. W. Casey, and C. R. McClain, "Recent trends in global ocean chlorophyll," Geophys. Res. Lett. **32**, L03606 (2005).
2. S. R. Signorini, B. A. Franz, and C. R. McClain, "Chlorophyll variability in the oligotrophic gyres: mechanisms, seasonality and trends," Front. Marine Sci. **2**, 1 (2015).
3. S. Sathyendranath, A. D. Gouveia, S. R. Shetye, P. Ravindran, and T. Platt, "Biological control of surface temperature in the Arabian sea," Nature **349**, 54–56 (1991).
4. M. J. Behrenfeld, W. E. Esaias, and K. R. Turpie, "Assessment of primary production at the global scale," in *Phytoplankton Productivity: Carbon Assimilation in Marine and Freshwater Ecosystems*, P. J. l. Williams, D. N. Thomas, and C. S. Reynolds, eds. (Blackwell Science Ltd., 2002), pp. 156–186.
5. J. O'Reilly, S. Maritorena, B. G. Mitchell, D. Siegel, K. L. Carder, S. Garver, M. Kahru, and C. McClain, "Ocean color chlorophyll algorithms for SeaWiFS," J. Geophys. Res. **103**, 24937–24953 (1998).
6. IOCCG, "Remote sensing of ocean colour in coastal, and other optically-complex, waters," in Reports of the International Ocean-Colour Coordinating Group, IOCCG Report Number 3, 2000, Vol. **3**, S. Sathyendranath, ed. (IOCCG, 2000).
7. IOCCG, "Remote sensing of inherent optical properties: fundamentals, tests of algorithms, and applications," in Reports of the International Ocean-Colour Coordinating Group, IOCCG Report Number 5, 2006, Vol. **5**, Z.-P. Lee, ed. (IOCCG, 2006).
8. A. Morel and L. Prieur, "Analysis of variations in ocean color," Limnol. Oceanogr. **22**, 709–722 (1977).
9. H. R. Gordon, D. K. Clark, J. W. Brown, O. B. Brown, R. H. Evans, and W. W. Broenkow, "Phytoplankton pigment concentrations in the

middle Atlantic bight: comparison of ship determinations and CZCS estimates," Appl. Opt. **22**, 20–36 (1983).

10. H. R. Gordon and A. Morel, *Remote Assessment of Ocean Color for Interpretation of Satellite Visible Imagery: A Review* (Springer-Verlag, 1983), p. 44.
11. R. W. Austin and T. J. Petzold, "The determination of the diffuse attenuation coefficient of sea water using the coastal zone color scanner," in *Oceanography from Space*, J. F. R. Gower, ed. (Plenum, 1981), pp. 239–256.
12. K. G. Ruddick, H. J. Gons, M. Rijkeboer, and G. Tilstone, "Optical remote sensing of chlorophyll a in case 2 waters by use of an adaptive two-band algorithm with optimal error properties," Appl. Opt. **40**, 3575–3585 (2001).
13. M. Darecki and D. Stramski, "An evaluation of MODIS and SeaWiFS bio-optical algorithms in the Baltic Sea," Remote Sens. Environ. **89**, 326–350 (2004).
14. H. R. Gordon, O. B. Brown, R. H. Evans, J. W. Brown, R. C. Smith, K. S. Baker, and D. K. Clark, "A semianalytic radiance model of ocean color," J. Geophys. Res. **93**, 10909–10910 (1988).
15. J. R. V. Zaneveld, "A theoretical derivation of the dependence of the remotely sensed reflectance of the ocean on the inherent optical properties," J. Geophys. Res. **100**, 13135–13142 (1995).
16. Z.-P. Lee, K. Du, K. J. Voss, G. Zibordi, B. Lubac, R. Arnone, and A. Weidemann, "An inherent-optical-property-centered approach to correct the angular effects in water-leaving radiance," Appl. Opt. **50**, 3155–3167 (2011).
17. R. Pope and E. Fry, "Absorption spectrum (380–700 nm) of pure waters: II. Integrating cavity measurements," Appl. Opt. **36**, 8710–8723 (1997).
18. J. A. Yoder and M. A. Kennelly, "Seasonal and ENSO variability in global ocean phytoplankton chlorophyll derived from 4 years of SeaWiFS measurements," Global Biogeochem. Cycles **17**, 1112 (2003).
19. A. Bricaud, A. Morel, M. Babin, K. Allali, and H. Claustre, "Variations of light absorption by suspended particles with chlorophyll a concentration in oceanic (case 1) waters: analysis and implications for bio-optical models," J. Geophys. Res. **103**, 31033–31044 (1998).
20. A. Morel and S. Maritorena, "Bio-optical properties of oceanic waters: a reappraisal," J. Geophys. Res. **106**, 7163–7180 (2001).
21. D. Antoine, D. A. Siegel, T. Kostadinov, S. Maritorena, N. B. Nelson, B. Gentili, V. Vellucci, and N. Guillocheau, "Variability in optical particle backscattering in contrasting bio-optical oceanic regimes," Limnol. Oceanogr. **56**, 955–973 (2011).
22. C. Le, C. Hu, J. Cannizzaro, D. English, F. Muller-Karger, and Z. Lee, "Evaluation of chlorophyll-a remote sensing algorithms for an optically complex estuary," Remote Sens. Environ. **129**, 75–89 (2013).
23. L. Qi, C. Hu, J. P. Cannizzaro, A. A. Corcoran, D. English, and C. Le, "VIIRS observations of a Karenia Brevis bloom in the northeastern Gulf of Mexico in the absence of a fluorescence band," IEEE Geosci. Remote Sens. Lett. **12**, 2213–2217 (2017).
24. A. A. Gitelson, D. Gurlin, W. J. Moses, and Y. Z. Yacobi, "Remote estimation of chlorophyll-a concentration in inland, estuarine and coastal waters," in *Advances in Environmental Remote Sensing*, Q. Weng, ed. (CRC Press, 2011).
25. G. Dall'Olmo, A. A. Gitelson, D. C. Rundquist, B. Leavitt, T. Barrow, and J. C. Holz, "Assessing the potential of SeaWiFS and MODIS for estimating chlorophyll concentration in turbid productive waters using red and near-infrared bands," Remote Sens. Environ. **96**, 176–187 (2005).
26. W. J. Moses, A. A. Gitelson, S. Berdnikov, V. Saprygin, and V. Povazhnyi, "Operational MERIS-based NIR-red algorithms for estimating chlorophyll-a concentrations in coastal waters—the Azov sea case study," Remote Sens. Environ. **121**, 118–124 (2012).
27. J. Gower, S. King, G. Borstad, and L. Brown, "Detection of intense plankton blooms using the 709 nm band of the MERIS imaging spectrometer," Int. J. Remote Sens. **26**, 2005–2012 (2005).
28. J. Gower, S. King, G. Borstad, and L. Brown, "Use of the 709 nm band of MERIS to detect intense plankton blooms and other conditions in coastal waters," in *Proceedings of the 2004 Envisat & ERS Symposium (ESA SP-572)* (2003).
29. C. Le, Y. Li, Y. Zha, D. Sun, and B. Yin, "Validation of a quasi-analytical algorithm for highly turbid eutrophic water of Meiliang Bay in Taihu Lake, China," IEEE Trans. Geo. Rem. Sens. **47**, 2492–2500 (2009).
30. K. L. Carder, F. R. Chen, Z. P. Lee, S. K. Hawes, and D. Kamykowski, "Semianalytic moderate-resolution imaging spectrometer algorithms for chlorophyll-a and absorption with bio-optical domains based on nitrate-depletion temperatures," J. Geophys. Res. **104**, 5403–5421 (1999).
31. C. Hu, Z. Lee, and B. Franz, "Chlorophyll a algorithms for oligotrophic oceans: a novel approach based on three-band reflectance difference," J. Geophys. Res. **117**, C01011 (2012).
32. T. S. Moore, M. D. Dowell, S. Bradt, and A. R. Verdu, "An optical water type framework for selecting and blending retrievals from bio-optical algorithms in lakes and coastal waters," Remote Sens. Environ. **143**, 97–111 (2014).
33. C. D. Mobley and L. K. Sundman, *HydroLight 5.2 User's Guide* (Sequoia Scientific Inc., 2013).
34. Z.-P. Lee, S. Shang, K. Du, and J. Wei, "Resolving the long-standing puzzles about the observed Secchi depth relationships," Limnol. Oceanogr. **63**, 2321–2336 (2018).
35. P. J. Werdell and S. W. Bailey, *The SeaWiFS Bio-Optical Archive and Storage System (SeaBASS): Current Architecture and Implementation* (Greenbelt, 2002).
36. Z.-P. Lee, Y.-H. Ahn, C. Mobley, and R. Arnone, "Removal of surface-reflected light for the measurement of remote-sensing reflectance from an above-surface platform," Opt. Express **18**, 26313–26342 (2010).
37. S. L. Shang, Q. Dong, Z. P. Lee, Y. Li, Y. S. Xie, and M. J. Behrenfeld, "MODIS observed phytoplankton dynamics in the Taiwan Strait: an absorption-based analysis," Biogeosciences **8**, 841–850 (2011).
38. P. J. Werdell and S. W. Bailey, "An improved bio-optical data set for ocean color algorithm development and satellite data product validation," Remote Sens. Environ. **98**, 122–140 (2005).
39. M. Szeto, P. J. Werdell, T. S. Moore, and J. W. Campbell, "Are the world's oceans optically different?" J. Geophys. Res. **116**, 604 (2011).
40. S. Sathyendranath, L. Lazzara, and L. Prieur, "Variations in the spectral values of specific absorption of phytoplankton," Limnol. Oceanogr. **32**, 403–415 (1987).
41. A. Bricaud, M. Babin, A. Morel, and H. Claustre, "Variability in the chlorophyll-specific absorption coefficients of natural phytoplankton: analysis and parameterization," J. Geophys. Res. **100**, 13321–13332 (1995).
42. Z. P. Lee, K. L. Carder, R. G. Steward, T. G. Peacock, C. O. Davis, and J. S. Patch, "An empirical algorithm for light absorption by ocean water based on color," J. Geophys. Res. **103**, 27967–27978 (1998).
43. Z. P. Lee, K. L. Carder, and R. Arnone, "Deriving inherent optical properties from water color: a multi-band quasi-analytical algorithm for optically deep waters," Appl. Opt. **41**, 5755–5772 (2002).
44. Z.-P. Lee, R. Arnone, C. Hu, P. J. Werdell, and B. Lubac, "Uncertainties of optical parameters and their propagations in an analytical ocean color inversion algorithm," Appl. Opt. **49**, 369–381 (2010).
45. F. Shen, Y. Zhou, and G. Hong, "Absorption property of non-algal particles and contribution to total light absorption in optically complex waters, a case study in Yangtze estuary and adjacent coast," Adv. Comput. Environ. Sci. **142**, 61–66 (2012).
46. S. Maritorena, D. A. Siegel, and A. R. Peterson, "Optimization of a semianalytical ocean color model for global-scale applications," Appl. Opt. **41**, 2705–2714 (2002).
47. M. Wang and W. Shi, "The NIR-SWIR combined atmospheric correction approach for MODIS ocean color data processing," Opt. Express **15**, 15722–15733 (2007).
48. W. Shi and M. Wang, "Characterization of particle backscattering of global highly turbid waters from VIIRS ocean color observations," J. Geophys. Res. **122**, 9255–9275 (2017).
49. W. Shi and M. Wang, "Ocean reflectance spectra at the red, near-infrared, and shortwave infrared from highly turbid waters: a study in the Bohai Sea, Yellow Sea, and East China Sea," Limnol. Oceanogr. **59**, 427–444 (2014).
50. Z. P. Lee and C. Hu, "Global distribution of case-1 waters: an analysis from SeaWiFS measurements," Remote Sens. Environ. **101**, 270–276 (2006).
51. H. M. Dierssen, "Perspectives on empirical approaches for ocean color remote sensing of chlorophyll in a changing climate," Proc. Natl. Acad. Sci. U.S.A. **107**, 17073–17078 (2010).